Resonant anti-Stokes Raman scattering in single-walled carbon nanotubes

Georgy Gordeev,[1,*] Ado Jorio,[2] Patryk Kusch,[1] Bruno G. M. Vieira,[1,3] Benjamin Flavel,[4,5] Ralph Krupke,[4,5] Eduardo B. Barros,[3] and Stephanie Reich[1]

[1]*Department of Physics, Freie Universität Berlin, Arnimallee 14, 14195 Berlin, Germany*
[2]*Department of Physics, Federal University of Minas Gerais, Belo Horizonte, Brazil*
[3]*Departamento de Física, Universidade Federal do Ceará, Fortaleza, Ceará, 60455-760, Brazil*
[4]*Institute of Nanotechnology, Karlsruhe Institute of Technology, Karlsruhe, Germany*
[5]*Institute of Materials Science, Technische Universitat Darmstadt, Darmstadt, Germany*

(Received 29 August 2017; published 18 December 2017)

The dependence of the anti-Stokes Raman intensity on the excitation laser energy in carbon nanotubes is studied by resonant Raman spectroscopy. The complete resonant anti-Stokes and Stokes Raman profiles of the high-energy longitudinal phonon (G^+) are obtained for (8,3), (7,5), (6,4), and (6,5) single chirality enriched samples. A high asymmetry between the intensity of the incoming and outgoing resonance is observed in the resonant Raman profiles. In contrast to Stokes scattering, anti-Stokes scattering is more intense at the outgoing resonance then at the incoming resonance. The resonance profiles are explained by a Raman process that includes the phonon-mediated interactions with the dark excitonic state. The chirality dependence of the Raman profiles is due to the variation in the exciton-phonon matrix elements, in agreement with tight-binding calculations. Based on the asymmetric Raman profiles we present the resonance factors for the Stokes/anti-Stokes ratios in carbon nanotubes.

DOI: 10.1103/PhysRevB.96.245415

I. INTRODUCTION

Single-walled carbon nanotubes are a unique material with outstanding mechanical and optical properties [1,2]. Their interaction with light is governed by excitons [3,4] with extremely high binding energies (up to ∼1 eV in a vacuum) and a complex structure of the excitonic states [5,6]. Interferences between excitonic states modify the optical responses of nanotubes such as absorption, photoluminescence, and photoconductivity [7,8]. Such interferences manifest indirectly in the resonance profiles of the nanotube Raman high-energy modes.

The high-energy modes of carbon nanotubes (G) comprise longitudinal (LO) and transverse (TO) phonons, labeled G^+ and G^- in semiconducting nanotubes. Resonant Raman scattering of the LO and TO modes reported an atypical asymmetric dependence of the Raman cross section on excitation energy. The asymmetry was found to depend on nanotube chirality [9–11]. The suggested mechanism to account for the varying cross-section of the incoming and the outgoing Raman resonance involves competing scattering channels between bright and dark excitonic states [10].

Anti-Stokes Raman scattering incorporates the same process for phonon absorption as Stokes scattering for phonon emission. Resonance profiles of anti-Stokes scattering will verify the proposed scattering pathways and deliver additional information about the photon-exciton and exciton-phonon coupling in nanotubes. Depending on the anti-Stokes Raman cross section, exciton resonances may potentially be exploited for phenomena like vibrational cooling [12–14] and generating correlated Raman photons [15,16].

Anti-Stokes spectra of the high-energy modes were previously reported at mixed chiralities concentrated powder, high temperatures, or plasmon-enhanced Raman scattering [17–19]. Despite the interest in anti-Stokes Raman scattering by the high-energy modes in nanotubes no systematic studies of their resonance profiles have been reported. This is due to the low intensity of the anti-Stokes process, which is proportional to the occupancy of the phonon branch. At room temperatures, the high-energy G modes of nanotubes are three orders of magnitude less intense in anti-Stokes than in Stokes scattering preventing measurements on individual nanotubes. As produced samples, on the other hand, contain many different chiralities with overlapping resonance profiles. The mixed response prohibits a detailed analysis of the resonance profiles as a function of chirality and diameter.

Here we report the anti-Stokes resonant behavior in the Raman profiles of chirality sorted single-walled carbon nanotubes. We measured four samples with (8,3), (7,5), (6,4), and (6,5) nanotubes, covered by sodium dodecyl sulfate (SDS) surfactant and suspended in an aqueous solution. In all the investigated chiralities we observe an asymmetry between incoming and outgoing resonances of the anti-Stokes signal of the high-energy LO mode. The Stokes and anti-Stokes resonance profiles are excellently described by a Raman scattering process involving interferences with the dark excitonic states. We calculate the ratio of the Stokes and anti-Stokes intensity depending on the energy difference between the bright exciton and the laser energy. The exciton-phonon matrix elements of different chiralities extracted from the experimental data qualitatively follow the behavior predicted by tight-binding calculations.

II. EXPERIMENT

The bulk samples for Raman experiments contained nanotubes coated by surfactant and suspended in an aqueous solution [20]. We used four chirality-enriched samples of the (8,3), (6,5), (6,4), and (7,5) nanotubes. The separation of

*gordeev@zedat.fu-berlin.de

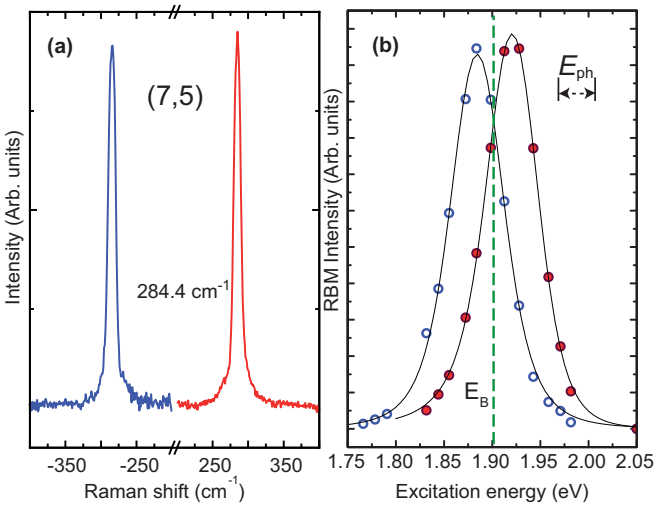

FIG. 1. Radial breathing mode of a (7,5) nanotube. The anti-Stokes spectrum is multiplied by the Boltzmann factor resulting in identical intensities for Stokes and anti-Stokes scattering. (a) Stokes and anti-Stokes components at $E_L = 1.9$ eV. (b) Stokes (filled symbols) and anti-Stokes (open symbols) Raman cross-sections versus excitation energy. Solid lines are fits by Eq. (1). The position of resonances determines the energy of the bright exciton, see Table I.

nanotubes was performed by a gel permeation chromatography [21]. Variation of the surfactant (SDS) concentration leads to the chirality selective absorbance of nanotubes to the gel. This method yields samples of single chirality species with up to 95% purity. The purity is verified by resonant Raman, where only a single radial breathing modes (RBM) peak appeared when varying the excitation energy over a large energy range, as well as absorption and photoluminescence spectroscopies as previously reported [21].

Resonance Raman spectroscopy was performed at room temperature for an excitation energy range from 1.63 to 2.4 eV. As excitation sources we used an Argon-Krypton, a Ti:sapphire, and a dye (Rhodamin 110, R6G, DCM) laser. The laser was focused by a macro lens (N.A. = 0.8) and the backscattered light collected. The scattered light was dispersed by a triple grating monocromator (Horiba T64000), equipped with 900 lines/mm gratings and detected by a charged couple device (CCD) detector. To exclude laser heating and related effects we varied the incident laser power by two orders of magnitude and no changes in counts per mW of anti-Stokes and in Raman shift were observed.

Simultaneously with the nanotube measurements, the Raman spectra of benzonitrile were obtained in the identical scattering geometry. For the calibration of the G and RBM modes we used molecular vibrations at ± 1589 cm^{-1} and ± 461 cm^{-1}, respectively. Benzonitrile has a constant Raman cross section [9,22] in the visible and near infrared wavelength range. Its vibrational level population is ruled by temperature. We verified this by comparing the Stokes and anti-Stokes intensities at the same spectral position, i.e., recording Raman spectra with a difference of $2\hbar w_{ph}$ between the excitation energies.

Important parameters for our analysis are the purity of the chirality-sorted samples and the exact energetic position of the exciton transitions. We determined the energy of the bright exciton for each nanotube chirality by resonant Raman spectroscopy of the RBMs. Figure 1(a) shows an example of the Stokes and anti-Stokes components of the (7,5) RBM at $\omega_{\mathrm{RBM}} = \pm 284$ cm^{-1}. The appearance of a single RBM peak verifies a successful single chirality enrichment of the sample. The RBM cross section exhibits a symmetric shape [23] due to the identical intensity of the incoming and outgoing resonance [24] [Fig. 1(b)]. The phonon energy is small, comparable to the width of resonance profile, therefore the incoming and outgoing resonances are not resolved. The maxima of the scattering efficiency are between the two resonances. The exciton energy is obtained by fitting the scattering intensity [4]:

$$I_{\mathrm{RBM}} \sim \left| \frac{M_1}{\left(E_L - E_B - i\frac{\Gamma}{2}\right)} - \frac{M_2}{\left(E_L - E_B - \hbar\omega_{\mathrm{RBM}} - i\frac{\Gamma}{2}\right)} \right|, \tag{1}$$

where E_L is the laser energy, E_B is the energy of the second exciton transition (bright exciton), $\hbar\omega_{\mathrm{RBM}}$ us the phonon energy, and $\frac{\Gamma}{2}$ represents the finite lifetime broadening. The first term in Eq. (1) is responsible for the incoming resonance, the second term for the outgoing resonance. To fit a symmetric cross-section we set the combined matrix elements $M_1 = M_2$. Separate fits of the Stokes and anti-Stokes resonance profiles yielded identical energy and lifetime broadening of the bright exciton, see Table I.

The transition energies (E_B) are comparable to previous studies, but are shifted to smaller energies [4,23] by 10 to 40 meV, see Table I. There are possibly two contributing mechanisms, bundling of the tubes and water molecules

TABLE I. Fitting parameters of the RBM resonance profiles. $\Delta E_B = E_B$ (this work)$-E_B$ (Ref. [23]), $\Delta w_{\mathrm{RBM}} = w_{\mathrm{RBM}}$ (this work)$-w_{\mathrm{RBM}}$ (Ref. [23]).

(n,m)	$2n+m$	Scatt. type	$\Gamma/2$ (meV)	E_B (eV) this work	E_B (eV) ± 10 meV Ref. [4,23]	ΔE_B (meV)	w_{RBM}(cm^{-1}) this work	w_{RBM} (cm^{-1}) Ref. [23]	Δw_{RBM} (cm^{-1})
(6,5)	17	anti-Stokes	60	2.155	2.18	–25	312.5	309.6	2.9
(7,5)	19	Stokes	41	1.902	1.92	–18	284.4	282.3	2.1
		anti-Stokes	42	1.902					
(8,3)	19	Stokes	59	1.822	1.86	–38	300.6	297.9	2.7
		anti-Stokes	52	1.824					
(6,4)	16	Stokes	47	2.098	2.11	–12	338.4	337.5	0.9
		anti-Stokes	52	2.097					

encapsulation. Encapsulation of water molecules induces a red shift of the transition energies ∼15 meV [25]. The selectivity of our enrichment method towards empty or filled nonanotubes is possible, but has not been studied yet. Bundling does not affect the frequency of the RBM [26], but water encapsulation is accompanied by a frequency upshift [25,27]. The difference between our measured RBM frequencies and previously reported values corroborates the water encapsulation mechanism as the dominant effect [4,23] (Table I). The remaining shift is due to the formation of small nanotube bundles. The (8,3) sample was most strongly affected with a bundling-induced shift of ∼25 meV.

III. THIRD- AND FIFTH-ORDER PERTURBATION THEORY OF THE RAMAN PROCESS IN CARBON NANOTUBES

One phonon Raman scattering in solid-state systems is commonly described by third-order perturbation theory [28]. The incoming and outgoing resonances are identical in intensity for a standard one-phonon process. One-phonon Raman scattering is insufficient to describe the asymmetric cross-sections of high-energy modes in semiconducting and metallic nanotubes [9,10,29]. Higher-order Raman processes were suggested to have an important contribution. They lead to fifth-order perturbation theory involving scattering between bright-dark and bright-bright excitonic states [10]. The dark excitons that participate in the Raman process of the high-energy modes are located at the K point of the Brillouin zone (BZ). Phonon-mediated interactions with the K-point excitons require phonons with a wave vector $q = \overline{\Gamma K}$ to couple to the bright state. These are the same modes that are responsible for the D mode in sp^2 carbons [30]. Additionally to the bright-dark exciton interactions to the fifth-order process contributes the scattering within the bright exciton, where the zero momentum LO phonons (G) are emitted and reabsorbed.

Figure 2(a) illustrates the scattering pathways corresponding to one of the possible Stokes (B) and anti-Stokes scattering processes (B'). In the Stokes process (B), the incident photon excites the bright exciton from the ground state (a). The exciton is scattered to the dark state by creating the K phonon (b). Then backscattering occurs, where the system gets to the same excited state of bright exciton by reabsorbing the K phonon (c). After that, the G phonon is created (d) and the bright exciton relaxes by emitting the photon of smaller energy.

The scattering via a dark exciton applies equally to Stokes and anti-Stokes processes; the K-point phonon is first created and then annihilated [Fig. 2(a)]. The probability of the inverse process of the interaction with the dark exciton is strongly reduced by the Boltzmann factor. In the anti-Stokes B' process, the time order is reversed compared to process B. The excited bright exciton absorbs a G phonon increasing its energy (a,b) then the emission (c) and the reabsorption of the K phonon takes place (d). Finally, the bright exciton relaxes by emitting the photon of higher energy.

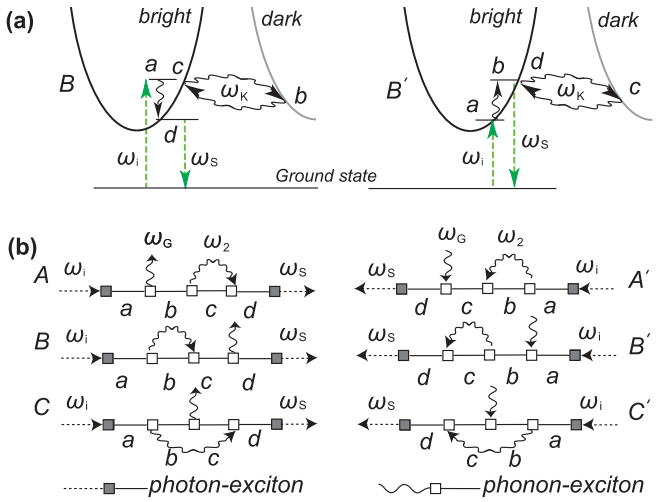

FIG. 2. Fifth-order Raman process. (a) Scheme of the scattering, corresponding to the Stokes B (left panel) and time reversed anti-Stokes B' (right panel) processes, with ω_K serving as ω_2. (b) Feymann diagrams (A–C) of the fifth-order contributions for Stokes and (A'–C') of the time-reversed processes for anti-Stokes Raman scattering.

The Feymann diagrams summarizing all contribution to the fifth-order process are depicted in Figure 2(b). The left panel shows the Stokes processes. The difference between the Stokes processes A–C arises from the multiple possible scattering sequence, where the scattering and backscattering (interference) between the excitonic states takes place at various steps of the third-order Raman process. The ω_2 phonon participating in the interference are ω_K and ω_G when scattered between bright-dark and bright-bright states, respectively. The right panel of Fig. 2(b) shows possible fifth-order anti-Stokes processes. For each A–C Stokes process there is a time reversed A'–C' anti-Stokes process with an inverted direction of the G phonon arrow. On vertexes, where in the Stokes process the G phonon is created in the anti-Stokes process phonon annihilation occurs. The combination of the third- and fifth-order processes results in Raman cross-sections $\sim|W_G|^2$ as a function of the laser energy [10]:

$$W_{G\pm}(E_L) = \frac{\left|M^{XL}_{B\Gamma S}\right|^2 M^{XP}_G}{(E_{B\Gamma S} - E_L)(E_{B\Gamma S} \pm \hbar\omega_G - E_L)}\left(1 + \frac{\left|M^{XP}_G\right|^2}{(E_{B\Gamma S} + \hbar\omega_G \pm \hbar\omega_G - E_L)(E_{B\Gamma S} + \hbar\omega_G - E_L)}\right.$$
$$+ \frac{\left|M^{XP}_G\right|^2}{(E_{B\Gamma S} - E_L)(E_{B\Gamma S} \pm \hbar\omega_G - E_L)} + \frac{\left|M^{XP}_K\right|^2}{(E_{\mathrm{DKS}} \pm \hbar\omega_G + \hbar\omega_K - E_L)(E_{B\Gamma S} + \pm\hbar\omega_G - E_L)}$$
$$\left. + \frac{\left|M^{XP}_K\right|^2}{(E_{\mathrm{DKS}} \pm \hbar\omega_G + \hbar\omega_K - E_L)(E_{B\Gamma S} + \hbar\omega_K - E_L)} + \frac{\left|M^{XP}_K\right|^2}{(E_{B\Gamma S} - E_L)(E_{\mathrm{DKS}} + \hbar\omega_K - E_L)}\right). \quad (2)$$

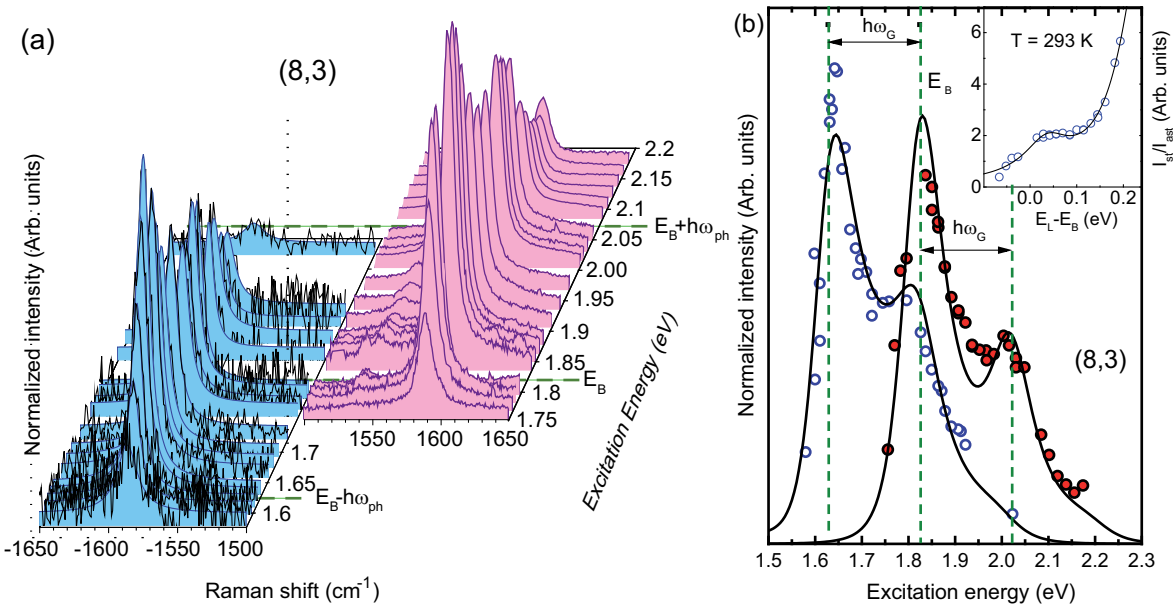

FIG. 3. G mode Stokes and anti-Stokes Raman spectra of (8,3) nanotubes. (a) Normalized Raman spectra covering the incoming and outgoing resonances. The anti-Stokes spectra include fits with a Lorentzian for clarity. (b) Excitation energy dependence of the LO phonon for Stokes (filled circles) and anti-Stokes (open circles) resonance scattering. The full lines are fits by Eq. (2). The dashed vertical lines represent the calculated positions on the incoming resonance at E_B and outgoing resonances at $E_B \pm \hbar\omega_G$. The open dots in the inset are the Stokes/anti-Stokes ratio plotted versus energy difference between the laser and the bright exciton ($E_L - E_B$). The line is a fit by Eq. (3) standing for the resonant correction factor.

M^{XL} is the exciton-photon and M^{XP} the exciton-phonon matrix element. The energy of the bright exciton is expressed as $E_{B\Gamma S} = E_B + i\Gamma_B/2$ and the energy of the dark exciton as $E_{\mathrm{DKS}} = E_D + i\Gamma_D/2$. $\Gamma_B(\Gamma_D)$ is the damping parameter associated with the lifetime of the bright (dark) exciton. $\hbar\omega_G$ is the phonon energy of the G mode observed in the experiment. $\hbar\omega_K$ represents the phonon energy involved in the coupling to the dark exciton. The positive sign of the phonon energy $\hbar\omega_G$ in Eq. (2) corresponds to the Stokes process, the negative sign to the anti-Stokes process. The first term in Eq. (2) describes the third-order process, the second and third terms describe fifth-order bright-bright scattering process, and the three last terms are due to the fifth-order bright-dark scattering process.

IV. EXPERIMENTAL RESULTS AND DISCUSSION

Figure 3(a) shows the Stokes and anti-Stokes Raman spectra of the G mode of an (8,3) nanotube, normalized as described in the experimental section. The energy range covers the resonance window of the second exciton transition at $E_{22} = 1.823$ eV. Both Stokes and anti-Stokes components of the strongest G^+ peak at ± 1584 cm^{-1} are observed on the spectra. The weaker G^- peak at ± 1540 cm^{-1} is observed only on the Stokes side due to its low intensity. The maxima in the scattering efficiency occur at excitation energies that match the incoming and outgoing resonances for this phonon mode, Fig. 3(b). The incoming resonance coincides with the energy of excitonic transition, while the outgoing resonances are shifted to higher (Stokes) and lower (anti-Stokes) excitation energies. The incoming Stokes resonance is higher in intensity than the outgoing Stokes resonance. This agrees with the asymmetric shapes of the Stokes cross-section previously reported in semiconducting and metallic nanotubes [9–11].

The anti-Stokes resonance profile shows a strong asymmetry between incoming and outgoing resonance, Fig. 3. Remarkably, the asymmetry between the resonances is inverted compared to Stokes scattering. The incoming

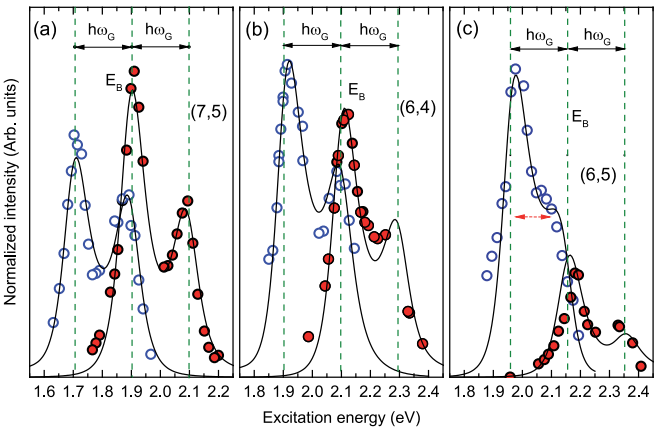

FIG. 4. The LO phonon Stokes (filled circles) and anti-Stokes (open circles) normalized Raman cross-sections of the single chirality (6,5), (7,5), and (6,4) samples. The vertical dashed lines correspond to the positions of the incoming and outgoing resonances obtained from the RBM analysis of E_{22} and measured phonon frequencies. The data are fitted by Eq. (2).

TABLE II. Constants for Stokes/anti-Stokes intensity ratios, Eq. (3).

(n,m)	y (meV)^2	C_1	C_2	Δ_1 (meV)	Δ_2 (meV)
(6,5)	1.22	1.69	3.64	45	180
(7,5)	2.03	1.57	13.6	31	187
(8,3)	3.6	1.33	10.09	35	248
(6,4)	3.1	1	4.6	28	170

resonance in the anti-Stokes profile is weaker than the outgoing resonance, as seen on the plot of the Raman cross-section versus laser energy in Fig. 3(b). Figure 4 shows the measured Raman cross-section of three additional chiralities (6,5), (7,5), and (6,4). The (8,3), (7,5), and (6,5) Stokes Raman profiles resemble the previously reported data [9], while the (6,4) Stokes profile is presented for the first time. The intensity ratios between incoming and outgoing resonances vary for the chiralities but overall the behavior is similar to the (8,3) tube in Fig. 3.

The reversed ratio in the intensity maxima of the Stokes and anti-Stokes is understood by considering time-reversal symmetry. When inverting the time order we turn A, B, and C processes into the A', B', and C' processes (Fig. 2). Considering $I_S(\omega_i,\omega_S) = I_{AS}(\omega_S,\omega_i)$ the equivalence between outgoing Stokes and incoming anti-Stokes becomes apparent. At frequencies corresponding to such resonances, the interference between the scattering channels in Eq. (2) is destructive and leads to a quenching of the Raman intensity.

The presence of multiple excitonic states and several scattering pathways in the Raman process shifts the positions of the intensity maxima away from incoming and outgoing resonances at E_B and $E_B \pm E_{ph}$ expected in two-level systems. The strength of the shift depends on the energetic separation of the excitons and the electron-phonon matrix elements. This shift is strongest in the (6,5) tube, where the intensity maxima of the anti-Stokes resonance profile are separated by only 130 meV compared to 196 meV phonon energy, as marked by horizontal dashed arrow on Fig. 4(c). Similar behavior was reported for armchair nanotubes [10].

Stokes and anti-Stokes intensities are crucial when evaluating the effective phonon temperature in carbon nanotubes by Raman scattering. The anti-Stokes/Stokes ratios are no longer exclusively dependent on temperature and resonance effects have to be considered [Fig. 3(b)]. We suggest a simplified empirical correction factor that depends on the energy of the bright exciton and the laser energies $\Delta = (E_L - E_B)$:

$$\frac{I_{\text{Stokes}}}{I_{\text{anti-Stokes}}}(T,\Delta) = \exp^{\frac{\hbar\omega_G}{KT}} \frac{|W_{G+}(E_L)|^2}{|W_{G-}(E_L)|^2} \cong \exp^{\frac{\hbar\omega_G}{KT}} \left(\frac{C_1 y}{y + (\Delta - \Delta_1)^2} + \frac{C_2 y}{y + (\Delta - \Delta_2)^2} \right), \quad (3)$$

where Δ_1 and Δ_2 correspond to the effective positions of the Stokes and anti-Stokes resonances. $2\sqrt{y}$ is the width of the combined profiles and C_1,C_2 are constants reflecting the varying intensity of the Raman resonances, see Table II. As shown in the inset of Fig. 3(b) the experimental results are reproduced by Eq. (3) in the regions where both signals are well detectable. It should be mentioned that the additional correction on ω^3 and spectrometer sensitivity need to be applied depending on the calibration procedure.

We now turn to analyzing the Stokes and anti-Stokes resonance profiles in the framework of third- and fifth-order perturbation theory, Eq. (2). We fit the Stokes and anti-Stokes resonance profile imposing identical exciton-phonon and exciton-photon matrix elements for both profiles from a single species. The energies of the bright excitons were taken from the RBMs measurements. For the energy splitting between dark and bright excitons we used values of the first excitonic transition E_{11} reported for all chiralities except the (6,4) nanotube, for which we use an average value of the other tubes [7,31]. The fitting parameters for all nanotubes are summarized in Table III. For the three SII tubes (7,5), (8,3), (6,4) $[(n-m)\text{mod}3 = -1]$ we obtain excellent fits of the Stokes and anti-Stokes resonance profiles. For the (6,5) the fitted Stokes resonance profile lies at lower energies compared to the experimental data, Fig. 4(c).

The exciton-phonon matrix element of the bright state is plotted in Fig. 5(a) as a function of the chiral angle. The matrix element of (7,5) is significantly smaller than in (8,3), (6,4), and (6,5). In the $2m + n = 19$ family the dramatic decrease of M_G^{XP} is corroborated by the tight binding calculation, performed according to Refs. [32–34] to verify this behavior. The calculated matrix element decreases from the (8,3) to the (7,5) tube by a factor of 24, in good agreement with the 30 times decrease obtained experimentally. The M_K^{XP} dependence on the chiral angle is shown in Fig. 5(b). We observe the same trend as M_G^{XP} in SII-type tubes, where the matrix element

TABLE III. Stokes (S) and anti-Stokes (a-S) fitting parameters of the G^+ Raman cross-sections with Eq. (2).

(n,m)	Scattering type	E_B (eV)	E_D (eV)	$M_{B\Gamma S}^{XL}$ (meV)	M_G^{XP} (meV)	M_K^{XP} (meV)	$\Gamma_B/2$ (meV)	$\Gamma_D/2$ (meV)
(6,5)	Stokes	2.155	2.184	83	195	140	75	72
	anti-Stokes	2.155	2.184	83	195	140	75	72
(7,5)	Stokes	1.902	1.938	764	7	130	73	37
	anti-Stokes	1.902	1.938	764	7	130	73	37
(8,3)	Stokes	1.822	1.855	115	154	152	84	52
	anti-Stokes	1.824	1.857	115	154	152	84	41
(6,4)	Stokes	2.098	2.131	71	152	321	90	229
	anti-Stokes	2.097	2.131	71	152	321	74	1400

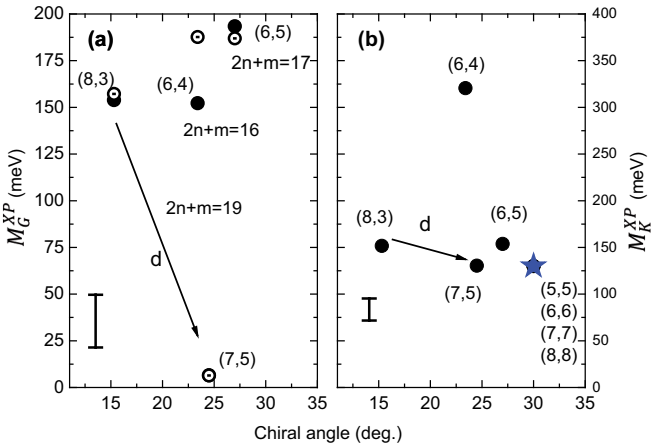

FIG. 5. Fitting parameters of the Stokes and anti-Stokes profiles versus chiral angle. (a) Bright exciton-phonon matrix element M_G^{XP} obtained from the experiment (filled dots) and calculated (open circles) [32–34]. Arrows indicate the direction along which d is increasing in single $2n+m$ nanotube family. (b) Dark exciton-phonon matrix element M_K^{XP}, filled circles our data, stars data for armchair nanotubes [10]. Vertical error bars show the averaged standard error.

decreases with the chiral angle. The matrix elements of achiral tubes in our experiment is close to the values reported for armchair (5,5), (6,6), (7,7), and (8,8) tubes [10].

The anti-Stokes component of the TO phonon (G^-) was not observed in the experiment due to the low Raman intensity. The asymmetry of the Stokes resonance profiles was previously reported to be similar as for the LO phonon with weak outgoing resonance [9,10]. We expect the TO anti-Stokes resonance profiles to qualitatively mimic the LO behavior with a different degree of asymmetry. The exciton-photon matrix element remains the same for TO and LO, but the exciton-phonon matrix element changes in the opposite direction within one $2n+m$ family [32].

The scattering between bright and dark excitons can be also realized by impurities. Defects can provide momentum to reinforce the interaction pathways and thus alter the asymmetry of the resonance Raman profile of nanotubes. The effect is similar to the double resonant Raman processes involved in the defect induced mode (D) [30]. Our experiments and past studies were performed on material with excellent crystal quality and low defects concentration. It would be interesting to perform similar experiments for more defective tubes to further advance our understanding of Raman scattering in nanotubes and, particularly, interactions between dark and bright excitons.

The strong outgoing anti-Stokes Raman resonances of carbon nanotubes point towards a path of engineering the population of selected phonon branches controlled by light. A population increase may be achieved at laser energies matching the outgoing Stokes resonance. Remarkably, for nanotubes a reduction of a phonon population may occur under certain conditions (phonon cooling). It requires the efficiency of the anti-Stokes process to overtake the efficiency of the Stokes process. We observed comparable intensities of the Stokes and anti-Stokes process at energy matching the outgoing anti-Stokes resonance for the (6,5) tube after normalization. In such excitation regimes, the phonon absorption is competing with the phonon emission, possibly allowing the phonon cooling to occur [14].

V. CONCLUSION

The anti-Stokes cross-section of the high-energy LO mode is measured in carbon nanotubes. The excitonic nature of the optical transitions alters the Stokes and anti-Stokes Raman scattering cross-sections. It results in strong incoming Stokes and outgoing anti-Stokes resonances, as we observe in four different semiconducting nanotube species (8,3), (7,5), (6,4), and (6,5). The resonance profiles successfully verified a model of quantum interferences between the third- and fifth-order scattering processes, involving phonon mediated interactions between excitonic states. The superposition of Stokes and anti-Stokes Raman cross sections yielded exciton-phonon matrix elements for various carbon nanotubes, in agreement with the tight-binding model. We suggest correction factors to account for resonance effect when evaluating the local temperature via the Stokes/anti-Stokes intensity ratio.

ACKNOWLEDGMENTS

We gratefully acknowledge the German Research Foundation (DFG via SFB 658, subproject A6). A.J. acknowledges financial support from the Humboldt Foundation. E.B.B. and B.G.M.V. acknowledge financial support from CAPES and CNPq. B.G.M.V. acknowledges the Coordenação de Aperfeiçoamento de Pessoal de Nivel Superior (CAPES) for the financial support under the program PDSE (Grant No. 88881.134611/2016-01) and Dahlem Research School (DRS).

[1] S. Reich, C. Thomsen, and J. Maultzsch, *Carbon Nanotubes: Basic Concepts and Physical Properties* (Wiley, New York, 2004).

[2] A. Jorio, R. Saito, G. Dresselhaus, and M. S. Dresselhaus, *Raman Spectroscopy in Graphene Related Systems* (Wiley, Weinheim, Germany, 2011).

[3] C. D. Spataru, S. Ismail-Beigi, L. X. Benedict, and S. G. Louie, Phys. Rev. Lett. **92**, 077402 (2004).

[4] J. Maultzsch, H. Telg, S. Reich, and C. Thomsen, Phys. Rev. B **72**, 205438 (2005).

[5] P. Avouris, M. Freitag, and V. Perebeinos, Nat. Photonics **2**, 341 (2008).

[6] V. Perebeinos, J. Tersoff, and P. Avouris, Nano Lett. **5**, 2495 (2005).

[7] O. N. Torrens, M. Zheng, and J. M. Kikkawa, Phys. Rev. Lett. **101**, 157401 (2008).

[8] X. Qiu, M. Freitag, V. Perebeinos, and P. Avouris, Nano Lett. **5**, 749 (2005).
[9] J. G. Duque, H. Chen, A. K. Swan, A. P. Shreve, S. Kilina, S. Tretiak, X. Tu, M. Zheng, and S. K. Doorn, ACS Nano **5**, 5233 (2011).
[10] E. H. Hároz, J. G. Duque, E. B. Barros, H. Telg, J. R. Simpson, A. R. Hight Walker, C. Y. Khripin, J. A. Fagan, X. Tu, M. Zheng, J. Kono, and S. K. Doorn, Phys. Rev. B **91**, 205446 (2015).
[11] L. G. Moura, M. V. O. Moutinho, P. Venezuela, C. Fantini, A. Righi, M. S. Strano, and M. A. Pimenta, Phys. Rev. B **89**, 035402 (2014).
[12] M. Steiner, H. Qian, A. Hartschuh, and A. J. Meixner, Nano Lett. **7**, 2239 (2007).
[13] J. Zhang, Q. Zhang, X. Wang, L. C. Kwek, and Q. Xiong, Nat. Photonics **10**, 600 (2016).
[14] G. Bahl, Nat. Photonics **10**, 566 (2016).
[15] A. Jorio, M. Kasperczyk, N. Clark, E. Neu, P. Maletinsky, A. Vijayaraghavan, and L. Novotny, Nano Lett. **14**, 5687 (2014).
[16] C. A. Parra-murillo, M. F. Santos, C. H. Monken, and A. Jorio, Phys. Rev. B **93**, 125141 (2016).
[17] S. D. M. Brown, P. Corio, A. Marucci, M. S. Dresselhaus, M. A. Pimenta, and K. Kneipp, Phys. Rev. B **61**, R5137 (2000).
[18] M. Steiner, M. Freitag, V. Perebeinos, J. C. Tsang, J. P. Small, M. Kinoshita, D. Yuan, J. Liu, and P. Avouris, Nat. Nanotechnol. **4**, 320 (2009).
[19] K. Kneipp, H. Kneipp, P. Corio, S. D. M. Brown, K. Shafer, J. Motz, L. T. Perelman, E. B. Hanlon, A. Marucci, G. Dresselhaus, and M. S. Dresselhaus, Phys. Rev. Lett. **84**, 3470 (2000).
[20] S. Lebedkin, F. Hennrich, T. Skipa, and M. M. Kappes, J. Phys. Chem. B **107**, 1949 (2003).
[21] B. S. Flavel, M. M. Kappes, R. Krupke, and F. Hennrich, ACS Nano **7**, 3557 (2013).
[22] Y. Piao, J. R. Simpson, J. K. Streit, G. Ao, M. Zheng, J. A. Fagan, and A. R. Hight Walker, ACS Nano **10**, 5252 (2016).
[23] C. Fantini, A. Jorio, M. Souza, M. S. Strano, M. S. Dresselhaus, and M. A. Pimenta, Phys. Rev. Lett. **93**, 147406 (2004).
[24] A. Jorio, A. G. Souza Filho, G. Dresselhaus, M. S. Dresselhaus, R. Saito, J. H. Hafner, C. M. Lieber, F. M. Matinaga, M. S. S. Dantas, and M. A. Pimenta, Phys. Rev. B **63**, 245416 (2001).
[25] W. Wenseleers, S. Cambré, J. Čulin, A. Bouwen, and E. Goovaerts, Adv. Mater. **19**, 2274 (2007).
[26] M. J. O'Connell, S. Sivaram, and S. K. Doorn, Phys. Rev. B **69**, 235415 (2004).
[27] S. Cambré, B. Schoeters, S. Luyckx, E. Goovaerts, and W. Wenseleers, Phys. Rev. Lett. **104**, 207401 (2010).
[28] P. Y. Yu and M. Cardona, *Fundamentals of Semiconductors Physics and Materials Properties* (Springer, Berlin, 1995).
[29] C. Thomsen and S. Reich, in *Light Scattering in Solids IX*, edited by C. Manuel and R. Merlin (Springer, Berlin, 2007), pp. 164–169.
[30] C. Thomsen and S. Reich, Phys. Rev. Lett. **85**, 5214 (2000).
[31] P. M. Vora, X. Tu, E. J. Mele, M. Zheng, and J. M. Kikkawa, Phys. Rev. B **81**, 155123 (2010).
[32] J. Jiang, R. Saito, K. Sato, J. S. Park, G. G. Samsonidze, A. Jorio, G. Dresselhaus, and M. S. Dresselhaus, Phys. Rev. B **75**, 035405 (2007).
[33] J. Jiang, R. Saito, G. G. Samsonidze, A. Jorio, S. G. Chou, G. Dresselhaus, and M. S. Dresselhaus, Phys. Rev. B **75**, 035407 (2007).
[34] J. Jiang, R. Saito, A. Grüneis, G. Dresselhaus, and M. S. Dresselhaus, Carbon **42**, 3169 (2004).